

Fourier transform electron spin resonance imaging

Uwe Ewert¹, Richard H. Crepeau, Curt R. Dunnam², Dajiang Xu, Sanghyuk Lee and Jack H. Freed

Baker Laboratory of Chemistry, Cornell University, Ithaca, NY 14853, USA

Received 17 May 1991; in final form 2 July 1991

Modern Fourier transform (FT) ESR methods have been combined with fast, high power pulsed magnetic field gradients to enable FT-ESR imaging. Spectral-spatial imaging by frequency and phase encoded FT methods are compared with cw methods. The initial phase encoded results are comparable in quality to those from the well-developed cw methods and further improvements which would enhance FT-ESR imaging are noted.

1. Introduction

ESR imaging is currently a very active area of research [1-3]. For the most part, ESR imaging is performed by cw methods. FT imaging is the method of choice in NMR, but it has been difficult to realize in ESR, because of its higher frequencies, much shorter relaxation times, and much greater spectral bandwidths. FT-ESR imaging offers several advantages over cw methods. First of all, data acquisition using FT methods can be much faster and the multiplex advantage can be used to enhance sensitivity. Secondly, in many cases, the image may be obtained by a straightforward FT, so that the calculation is significantly faster than back-projection, which may require time-consuming interpolation and digital filtering to minimize artifacts [4]. Third, FT methods sample an evenly spaced grid of points, whereas back-projection, requiring a polar to Cartesian coordinate transform, may introduce distortion and artifacts [5]. Also avoided are other sources of inaccuracy in cw imaging, including passage effects due to fast sweep rates, overmodulation of the signal, saturation and artifacts resulting from the missing angles because of limits on the maximum gradient available. A fourth advantage, appropriate to the use of our

phase encoding FT methods (cf. below), is that the gradient pulse duration is fixed, so that relaxation effects remain the same for each point in the experiment [6].

FT imaging may also provide significantly greater combined spectral and spatial resolution than cw imaging. Spectral-spatial imaging [3,4,7-9] provides the ESR spectrum as a function of position in the sample, which is of considerable value as demonstrated in several recent cw-ESR experiments [1,2,10-12]. In phase-encoding FT methods, the spatial resolution depends on both the amplitude and duration of the gradient pulse [13], whereas the resolution of cw imaging is limited by the maximum available gradient [6]. Finally, FT imaging is much more flexible with respect to the possible combination of dimensions (both spectral and spatial) that can be presented in the final image. For example, one could perform two- (spectral) dimensional ESR in combination with one or more spatial dimensions. Thus modern 2D-FT-ESR methods [14-19] such as 2D-ELDOR could provide the ESR capability of measuring molecular dynamics as a function of spatial coordinate.

FT-ESR [14-25] presented major instrumental challenges compared to FT-NMR, but it has recently been developed to the point where it can be applied to ESR spectra extending over 100-250 MHz, requiring nanosecond time resolution [14-16]. Such time resolution is also useful for short FIDs, such as

¹ Currently at Centre of Scientific Instruments of the Academy of Sciences of the DDR, Berlin.

² Laboratory of Nuclear Studies, Cornell University, Ithaca, NY.

arise from spin dephasing due to large magnetic field gradients, and if FIDs become too short one can detect the echo decay [17]. The major remaining technical challenge of FT-ESR imaging experiments was to achieve intense but rapidly pulsed magnetic field gradients at the sample, which requires rapid switching of the very high currents needed to drive the gradient coils.

We report in this work our successful realization of FT-ESR imaging. This includes frequency encoding as well as phase encoding FT-ESR, and the application to spectral-spatial ESR imaging. The realization of 2D-ELDOR imaging as well as FT-ESR imaging based on spin echoes is described in an accompanying Letter [26].

Prior applications of pulsed ESR to imaging, which for the most part involved constant gradients or the equivalent, have been reviewed [3,27]. Most relevant to this work is an experiment by Mehring and co-workers who sampled the amplitude of the FID at a single fixed time just after a pulsed field gradient, which was stepped in order to obtain a high resolution image. This application relied on the very long relaxation time T_2 of the fluoranthenyl single crystals [28]. Milov et al. [29] report a phase encoded imaging experiment using a pulsed field gradient between two pulses of an electron spin echo experiment with measurement of the peak amplitude of the echo, and Sloop et al. report on a closely related experiment [30].

2. Methods

Our FT-ESR spectrometer is described elsewhere [15–17]. It is based on simultaneous collection of both quadrature components of the FID. In order to avoid phase corrections due to (1) finite deadtime and (2) off-resonance effects arising from finite microwave fields, we display magnitude spectra [15–17]. We describe below the new features of the imaging experiment.

2.1. Sample

The sample was chosen to provide a clear demonstration of the imaging capability of our pulsed FT-ESR spectrometer, and to demonstrate the addi-

tional information [26] that can be obtained with FT experiments. The sample consisted of two adjacent tubes, shown in fig. 1a. These samples will show a 3 line (^{14}N) and a 2 line (^{15}N) cw spectrum respectively, clearly distinguishing them in spectral-spatial imaging experiments. The concentrations chosen are sufficient to allow significant Heisenberg exchange to take place within the T_1 and T_2 relax-

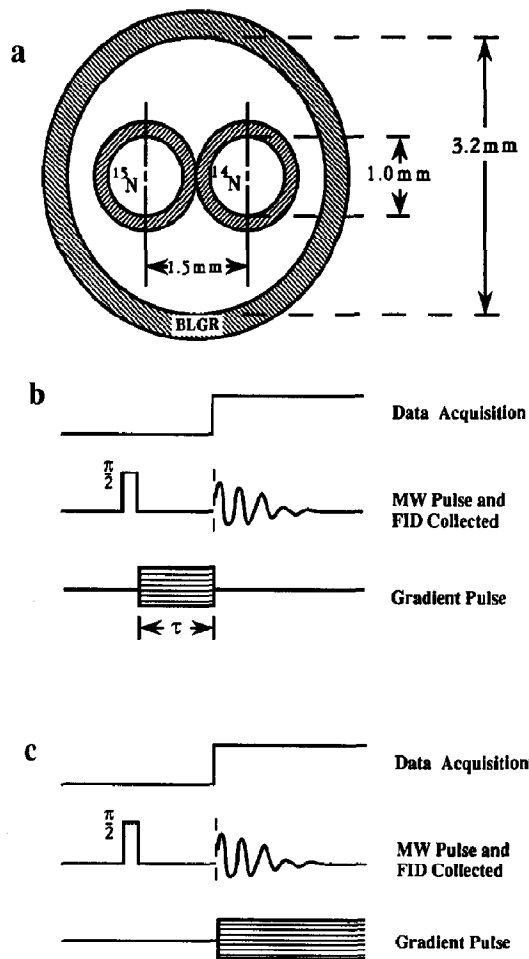


Fig. 1. (a) Sample tube arrangement used in the pulsed gradient phase and frequency encoded experiments. The tubes contain 4.5 mM ^{14}N perdeuterated tempone (PDT) and 4.0 mM ^{15}N tempone in dodecane and are within the bridged loop-gap resonator (BLGR) [16]. (b) The phase encoding pulse sequence. The gradient pulse was stepped from -80 to $+80$ G while the FID shown was collected following the gradient pulse. (c) The frequency encoding pulse sequence. The stepped gradient was applied only during data collection to minimize dephasing during the deadtime following the microwave (MW) pulse.

ation times. The sample tubes fit easily into our 3.2 mm inner diameter bridged loop-gap resonator described previously [16–18].

2.2. Gradient coil construction

Pulsed gradient imaging requires fast rise and fall times, high peak gradient values, good coupling to the pulse driver and uniform gradients. All aspects of the pulsed gradient system had to be considered simultaneously to insure proper working of the final design. The gradient rise and fall times depend on the maximum applied voltage across the coils and the coil inductance. The driver rise and fall times must also be figured into this calculation as well as the cable connecting the driver and coils. Our goal in this initial design effort was rise and fall times of 45 ns or better for a maximum gradient of 100 G/cm.

Construction of our gradient coil was based on the method described by Suits and Wilken [31]. The gradient is generated by a set of discrete current paths mounted on the cylindrical pyrex glass shield of the resonator and aligned along the x axis (cf. fig. 2a). The z component of the magnetic field for four single infinitely long current paths at $\pm\theta, \pi\pm\theta$ is given by

$$B_z(y, z) = h_{01}z + h_{03}(z^3 - 3y^2z) + h_{05}(z^5 - 10y^2z^3 + 5y^4z) + \dots, \quad (1)$$

where $h_{0m} = -(2\mu_0 NI / \pi R^{m+1}) \sin[(m+1)\theta]$. Here m is odd, N is the number of turns of wire, I is the current per turn, R is the radius of the cylinder. The actual coils are driven in parallel over connecting lines not shown and must form closed loops. We chose $K = 1.5R = 10.5$ mm so that the effects from the finite length and arcs are negligible [31], and we set $\theta = 45^\circ$ to eliminate the $\sin 4\theta$ term and thereby maximize the volume of linear magnetic field gradient. Ignoring higher order terms, we obtain a linear gradient

$$G = \partial B_z / \partial z = -2\mu_0 NI / \pi R^2. \quad (2)$$

The gradient is expected to be linear to 1% over an area of $\pi(0.21R)^2$ in the yz plane that can easily contain our sample. Minimizing the inductance (L) of this coil and the number of turns are essential con-

siderations since $dG/dt \propto L^{-1} \propto N^{-2}$. We used a single turn to minimize L , and we compensated by increasing the current I to get the desired gradient within the available power supply specifications. From eq. (2) we predict a gradient of about 1.6 G/cm A. Our measurements at $I = 60$ A give $G = 1.2$ G/cm A and $L = 0.2$ μ H.

2.3. Fast gradient coil driver (FGCD)

Design specifications for a fast driver section are in essence prescribed by the gradient coil assembly surge impedance, the requisite field intensity and the maximum acceptable gradient rise and fall times. For the system described here a driver output peak current of 75 A and peak voltage level of 500 V are required. Under these conditions, peak field charging powers of approximately 40 kW must be produced. The stringent requirements that our pulsed gradient experiments place on the gradient amplitude and switching times preclude the use of earlier pulsed gradient [28–30] or switched field [32–34] schemes, which are unsuitable either because of insufficient maximum gradient or slow transition times or both. To achieve gradient field rise and fall times of 45 ns, we found it necessary to conduct a series of detailed SPICE [35] simulations of candidate driver topologies and associated power output device types. Of the several techniques considered, a power MOS-FET driver and saturated-mode output array implementation was chosen for superiority in providing variable pulse width, fast rise time, and a good approximation to rectangular pulse shape.

Mechanical constraints were significant factors in the fast driver design process. Because the cavity's gradient coil assembly presents an essentially reactive electrical load impedance, the FGCD must be located in close proximity to it. This consideration requires that the driver module be located within the magnet yoke. Consequently, to preserve magnetic field homogeneity, we found it necessary to specify, to the extent possible, non-magnetic materials in its construction. Steady-state heat dissipation, which can reach several hundred watts under maximum repetition rate and gradient field conditions, required that the driver enclosure design incorporate a water-cooled copper baseplate.

Fig. 2b shows the FGCD system. The functions of

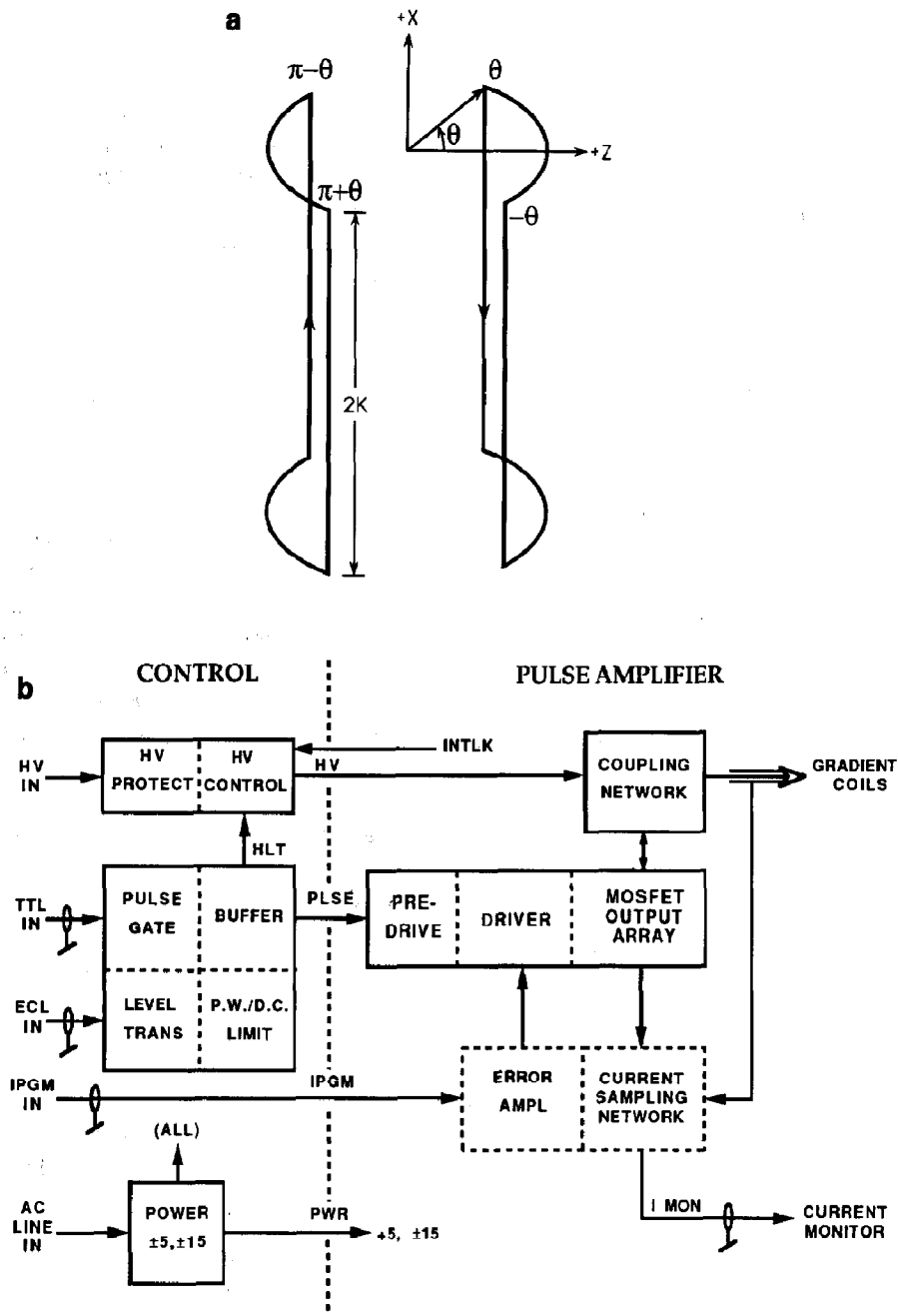


Fig. 2. (a) The coil configuration used in the pulsed gradient experiments. The coil is mounted on the outside of the pyrex glass shield for the bridged loop-gap resonator. The shield was painted on the inside with a thin layer of silver paint that allowed passage of the gradient pulse to the sample and yet contained the microwave energy applied to the resonator. Five horizontal grooves were cut in this silver paint to reduce eddy current effects. (b) Block diagram of the fast gradient coil driver system. Input pulses (TTL in and ECL in) are translated (if ECL), tested against preset width and duty factor limit values (HLT turns off the high voltage for protection), buffered and routed to the pulse amplifier module (PAM). The PAM is located within 20 cm of the loop-gap resonator gradient coil assembly to minimize transmission line effects resulting from the higher reactive nature of the load. (Note it is intrinsically impossible to match over the broadband spectrum of the short gradient pulse.) Pulses are amplified to provide large peak currents necessary for rapidly switching the high-power output MOSFET array. This array controls the gradient coil pulsed current and is designed to provide rapid turn-on and turn-off times. An output Coupling Network interconnects the programmable high voltage supply (Electronic Measurements inc. model TCR 600S1, 500 V, 0-1 A), output MOSFET array, and the transmission line to the coils. This network allows for dc decoupling of the load, a fixed maximum pulse energy, and controlled energy recapture during collapse of the gradient field. An insulated triplanar stripline of 6.5Ω characteristic impedance and 50 kW peak power capability connects to the coil assembly. Output current during operation is sampled and appears at a BNC connector on the driver module.

this unit are to interface the computer control signals with the high voltage supply, provide fast, high power pulses to the gradient coils, insure protection for sensitive components, and, through a system of interlock switches, to protect the user from potentially dangerous voltages.

Output network component values have been optimized by SPICE simulation for critical damping with the measured value of gradient coil inductance. Careful SPICE analysis and matching of interstage coupling parameters has yielded prototype rise and fall times within limits initially specified for the FT imaging system.

Experience to date with this single-channel pulse amplifier demonstrates that output pulses of satisfactory peak current level, rise time and predictable form are consistently achieved. A major upgrade, to suppress parasitic inductance and improve pulse shape, will replace computer control of the high voltage supply by a computer controlled active feedback loop as indicated within the dashed outline in fig. 2b (IPGM). Preliminary SPICE simulations predict that driver operation in an active feedback mode will permit imaging spectroscopy with precisely defined constant-current pulses of 60 ns minimum fwhm at peak field-charging levels approach 100 kW. This will correspond to rise and fall times for the field gradient of 30 ns resulting from a combination of higher voltage and reduced inductance obtained by positioning the coils on the inside of the resonator shield. (Our present open-loop operating mode is characterized by rise and fall times for the field gradient of slightly less than 45 ns but also by ripple in the gradient amplitude near the pulse edges, an effect which presently limits resolution in the frequency encoded experiments, but which the upgrade would address.) The maximum repetition rate due to heating effects for the coils is 50 kHz and for the driver circuit is 2 kHz. Our active feedback design will raise the driver limit also to 50 kHz enabling more rapid data collection.

2.4. Theoretical expressions

The pulse sequences of the experiments reported here are shown in fig. 1. The phase encoded single pulse experiments (fig. 1b) rely on the deadtime period, between the $\pi/2$ microwave pulse and the col-

lection of the free induction decay (FID) signal for phase encoding the magnetization with a gradient pulse, G , varying from $-G_{\max}$ to G_{\max} G/cm applied parallel to the dc magnetic field (z direction). Let $S_0(t_1, c(x))$ be the complex FID signal at time t_1 after the $\pi/2$ pulse with no field gradient applied. Its real part represents the in-phase component, and its imaginary part the component in quadrature. It is normalized such that at $t_1=0$, $S_0(0, c(x)) = \text{Re } S_0(0, c(x)) = 1$. Note that S_0 is, in general, a function of position x , due to its possible dependence on concentration $c(x)$. Now if a field gradient G is applied for a period τ just after the $\pi/2$ pulse we have the observed signal for $t_1 > \tau$

$$\bar{S}_p(t_1, G) = \int_{-\infty}^{\infty} c(x) \exp(-ikx) S_0(t_1, x) dx, \quad (3)$$

where we have $k = \gamma_e G \tau$. The Fourier inverse of eq. (3) is

$$c(x) S_0(t_1, x) = (1/2\pi) \times \int_{-\infty}^{\infty} \exp(ikx) \bar{S}_p(t_1, k/\gamma_e \tau) dk, \quad t_1 > \tau. \quad (4)$$

If we now FT with respect to t_1 (which is best done after correcting for the spectral "deadtime" τ , e.g. by linear prediction (LP) [16]), we obtain: $c(x) \bar{S}_0(f, x)$ where $\bar{S}_0(f, x)$ is the FT of $S_0(t_1, x)$ and corresponds to the cw spectrum of the spins located at position x . (The real part of $\bar{S}_0(f, x)$ is the absorption and the imaginary part the dispersion in an ideal experiment [15-17].) Now $c(x) \bar{S}_0(f, x)$ represents the spectral-spatial image obtained by the method of phase encoding. The actual concentration distribution $c(x)$ may be obtained from eq. (4) by extrapolating back to $t_1=0$ (e.g. by LP) or from $c(x) \bar{S}_0(f, x)$, corrected for deadtime, by integrating it over f , since $\int \bar{S}_0(f, x) df = S_0(0, x) = 1$. (Actually, the limits in eq. (4) are determined by $k_{\max} = \gamma_e G_{\max} \tau$, the experimental limit in k space, but we may hope to improve resolution by using LP in k space.)

It follows from eq. (4) that the nominal spatial resolution which merely sets a theoretical bound (i.e. is twice the point to point spacing after fast FT), will be $\delta x \approx 1/\gamma_e G_{\max} \tau$ (see also ref. [28]). However, the

real resolution will clearly depend on the signal to noise ratio (S/N) in an actual experiment (including any artifacts in the method). For example, if k_{\max} is increased sufficiently, T_2^* will decrease to the point where the spins are so rapidly dephased in the rotating x - y plane that no FID can be observed above the noise level and hence one no longer improves the actual resolution. In the work presented here, the short gradient pulse width insures that k_{\max} is not too large (cf. fig. 3).

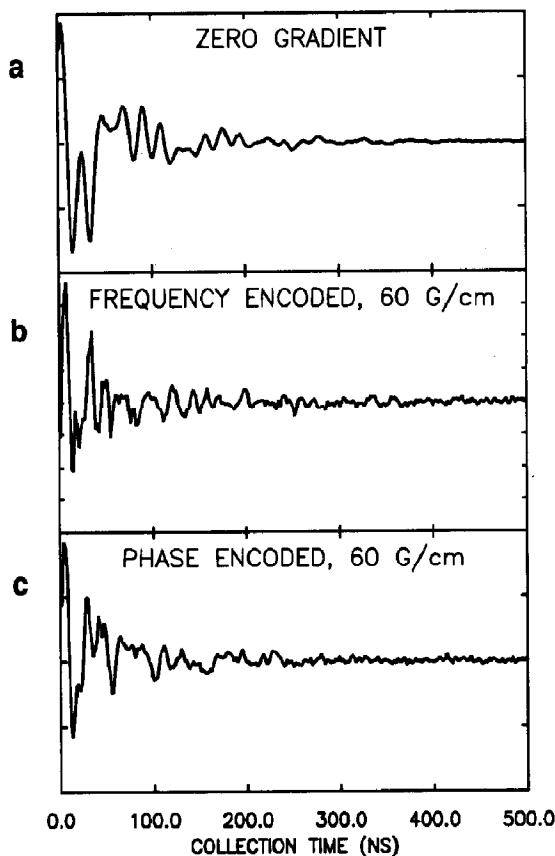


Fig. 3. In-phase FID data from sample of fig. 1a after an applied 5.5 ns $\pi/2$ pulse. (a) FID in the absence of gradient. (b) FID with pulsed gradient of 60 G/cm, turned on within 5 ns of the start of data collection, as in fig. 1c, showing reduced T_2^* (note the plots are normalized to the maximum value). (c) FID of phase encoded experiment with gradient of 60 G/cm; the gradient is applied as in fig. 1b and the data are collected after turning off the gradient. In these cases deadtime, averaging and sampling time are as in fig. 4 except that 3 such FIDs have been further averaged in this figure. The observed spectral coverage is flat over a bandwidth of 160 MHz and extends to 200 MHz with a maximum of 50% reduction of signal in the wings.

The frequency encoded experiment of fig. 1c measures the FID while the gradient is applied. Here the position of the spins is encoded by their precession frequency in the FID. We have the observed signal

$$\bar{S}_f(t_1, G) = \int_{-\infty}^{\infty} c(x) \exp(-i\gamma_e G_x t_1) S_0(t_1, x) dx. \quad (5)$$

Here both the phase factor and the S_0 depend on t_1 and in general on x . This results in the need to use a polar to Cartesian transform and 2D-FT [5] or back-projection methods [4,7-9] to separate the spectral and spatial parts. The spectral-spatial image is similar to that of the phase encoded experiment, and the nominal resolution is given by $\delta x \approx 1/\gamma_e G_{\max} T_2^*$ [3,28] due to the T_2^* determining the effective time of the FID experiment. (Note here that T_2^* depends upon G .) Here again the practical limit to the applied gradient depends on the sample and signal to noise considerations. The back-projection leads to high pass artifacts due to the deadtime which influences mainly the spatial distribution. The polar to Cartesian transform followed by 2D-FT method should restrict the distortions to the spectral component. When $S_0(t_1, x)$ is independent of x as in the case of a small concentration of spins, we have

$$\bar{S}_f(t_1, G) = S_0(t_1) \tilde{c}(\gamma_e G t_1) \quad (6)$$

or for each value of t_1 we get another value of $\tilde{c}(k)$, where now $k = \gamma_e G t_1$.

Eqs. (5) and (6) apply to the case of constant gradients. With a pulsed gradient it is possible to reduce the effect of shortening T_2^* , by applying the gradient only after τ_d , the spectrometer deadtime, in which case the argument of the exponent in eq. (5) is replaced by: $-i\gamma_e G_x (t_1 - \tau_d)$ with equivalent change in eq. (6). The image reconstruction can now be performed by back-projection from the magnitude spectrum without spatial high pass artifacts and with sensitivity enhancement.

3. Results and discussion

Initial efforts [36] were based on stationary gra-

dients for frequency encoding experiments (using gradient coils described elsewhere [36,12]). As discussed in section 2, a constant gradient leads to a shortening of T_2^* . When $T_2^* \ll \tau_d$, no FID will be observed; so this limits the maximum gradient, hence the resolution. Unfortunately, the effects of a finite τ_d lead to reduced S/N and artifacts in the general case. Nevertheless, it was possible to demonstrate 2D spatial-spatial FT-ESR imaging on a sample consisting of two thin dots of DPPH separated by 2.8 mm [36]. The maximum gradient that could be used was 20 G/cm and projection reconstruction [4,7-9] was utilized. (One way to overcome the deadtime problem, that is appropriate for inhomogeneously broadened spectra, is to use spin echoes as discussed in the accompanying Letter [26].)

It was possible, with pulsed gradients, to improve the frequency encoding experiment. We used the pulse scheme corresponding to fig. 1c applied to the sample of fig. 1a. Here the rising gradient edge is synchronized with the start of the data acquisition, yielding a considerably higher intensity and S/N than the stationary gradient FID, so it is possible to apply larger gradients. The synchronization of the rising pulse with the data acquisition was better than 5 ns and was accomplished with a test sample of known distribution of spins. The less than 45 ns risetime and the initial ripple of the gradient pulse appear to minimally affect the imaging when this adjustment is made, perhaps because the FID is collected out to several hundred nanoseconds. No corrections in the analysis were made for the gradient pulse shape.

We applied this pulsed gradient method to spectral-spatial FT-ESR imaging (cf. fig. 1c), which involves measuring the FID (cf. fig. 3) repeatedly with different gradients. Although every FID is frequency encoded in the gradient (or k) dimension, the FIDs, for different G , are phase encoded with respect to each other, (cf. eq. (5)). The gradients were stepped from the maximum available gradient of +80 G/cm to the minimum of -80 G/cm. The spectral-spatial analysis was performed by filtered back-projection and interpolation of missing projections in analogy with the well known cw algorithms [4,7-9]. We used 91 actual (and 9 missing) projections according to the expression $G = (\Delta S / \Delta R) \cot \alpha$, where ΔS is the spectral width, ΔR is the size of the object and α is the angle of rotation of the pseudo-object for a target

matrix. Also the 4 step CYCLOPS phase cycle was used to cancel mismatched quadrature arm artifacts [15,16]. The result of the reconstruction is shown in fig. 4a.

For comparison, we performed a cw spectral-spatial imaging experiment on the same sample using the cw-imaging spectrometer described elsewhere [12,36]. The gradient was varied from -550 to +550 G/cm with 91 actual projections (with an additional 9 higher gradients interpolated). The total measuring time was 7 min, comparable to the FT-ESR experiment. This cw image is of high quality, cf. fig. 4b. The FT-ESR image shows poorer resolution, especially in the spatial regime. This is not surprising considering that the maximum gradient in the cw experiment was 7 time greater. (The nominal resolution of the cw spectral-spatial experiment is 130 μm whereas that for the FT-ESR experiment is 600 μm [37].) An additional blurring of the FT-ESR result is expected due to distortions from the assumed rectangular gradient pulse shape. Also, as a result of finite τ_d , the shorter T_2^* of the ^{15}N sample caused its spectrum to be reproduced with similar intensity relative to the T_2^* of the perdeuterated ^{14}N sample.

The application of phase encoding gradients according to fig. 1b improving the image quality, first of all because only the integral over the pulse is the relevant parameter and not the pulse shape. In this scheme the gradient pulse was applied for 90 ns (during τ_d) immediately after the microwave pulse, and the data acquisition was initiated following τ_d . Typical FIDs are shown in fig. 3. According to eqs. (3) and (4) the 2D-FT reconstructs the desired spectral-spatial image. While the spectral distribution is affected by the deadtime, the spatial distribution is unaffected. In the present experiment, the spectrum consists of lines that are Lorentzian, so the effect of finite τ_d can be neglected (the different T_2^* 's of the two spectra only affect the relative intensities, cf. above). (Recall, $\delta x \approx 1/\gamma G_{\text{max}} \tau$ by which we obtain $\delta x \approx 80 \mu\text{m}$).

Fig. 4c shows the FT-ESR image collected in 9 min. It shows significantly better actual resolution than the frequency encoded experiments. The S/N is comparable to the benchmark cw experiment. The surprisingly good sensitivity results partially from the multiplex advantage of 16 resulting from the $16^2 = 256$ points collected following each pulse train

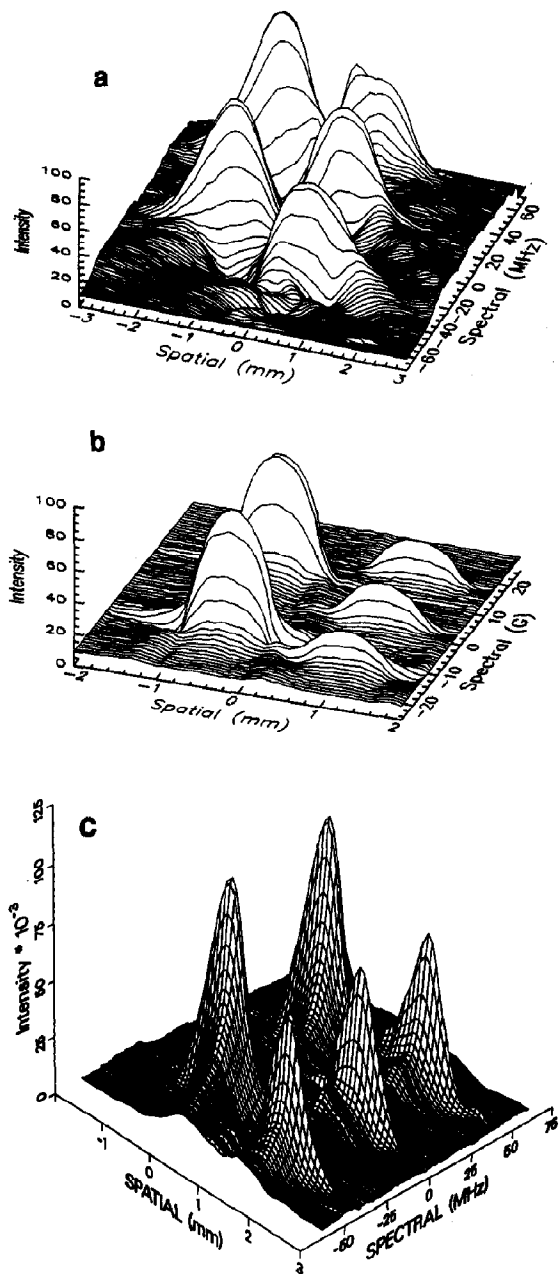


Fig. 4. Surface plots of the spectral-spatial experiments discussed in the text. (a) Pulsed spectral-spatial frequency encoded experiment. The sample is shown in fig. 1a and the pulse sequence of fig. 1c was used. The gradient range was ± 80 G/cm. (b) cw analogue of (a). This cw spectral-spatial image was taken with constant gradients upto ± 550 G/cm. (c) Pulsed spectral-spatial phase encoded image. These are magnitude spectra. The gradient range was ± 80 G/cm; the deadtime (τ_d) was 110 ns; 64 averages were performed for each step of the 4 step CYCLOPS [15,16] phase cycle sequence; and a 2 ns sampling time was used.

compared to collection of data at each magnetic field value during a cw field sweep.

We believe that these results are very encouraging for the future of phase encoded FT-ESR imaging. For example, by utilizing a faster signal averager (DSP Technology model 2102SA modified for interleaving successive sweeps [16]) we have very recently increased our data acquisition rate by a factor of 100 over that utilized in the experiments reported here (where an HP 54100A sampling oscilloscope [15,16] was used). Furthermore, we have yet to optimize the FT-ESR imaging methods, e.g. by improving gradient pulse shape, stability and linearity; reducing pulse rise/fall times; and by increasing maximum gradients. Such technical developments as these will greatly enhance the capabilities of FT-ESR imaging.

Acknowledgement

We thank Dr. David E. Budil for his 3D graphics efforts. This work was supported by NSF Grants DMR89-01718 and CHE90-04552 and NIH Grant GM-25862.

References

- [1] EPR imaging and in vivo EPR, eds. G.R. Eaton and S.S. Eaton (CRC Press, Boca Raton), in press.
- [2] Proceedings of the International Workshop on In Vivo ESR and ESR Imaging, *Physica Medica V* (1989) pp. 63-335.
- [3] S.S. Eaton and G.R. Eaton, in: *Modern pulsed and continuous-wave electron spin resonance*, eds. L. Kevan and M. Bowman (Wiley, New York, 1990) ch. 9.
- [4] M.M. Maltempo, S.S. Eaton and G.R. Eaton, *J. Magn. Reson.* 77 (1988) 75.
- [5] R.R. Ernst, G. Bodenhausen and A. Wokaun, in: *Principles of nuclear magnetic resonance in one and two dimensions* (Oxford Univ. Press, Oxford, 1990).
- [6] P. Mansfield and P.G. Morris, in: *NMR imaging in biomedicine* (Academic Press, New York, 1982) ch. 5.
- [7] U. Ewert and T. Herrling, *Chem. Phys. Letters* 129 (1986) 516.
- [8] M.M. Maltempo, *J. Magn. Reson.* 69 (1986) 156.
- [9] M.M. Maltempo, S.S. Eaton and G.R. Eaton, *J. Magn. Reson.* 72 (1987) 449.
- [10] E.D. Stemp, G.R. Eaton, S.S. Eaton and M.M. Maltempo, *J. Phys. Chem.* 91 (1987) 6467.
- [11] R.K. Woods, J.W. Dobrucki, J.F. Glockner, P.D. Morse II and H.M. Swartz, *J. Magn. Reson.* 85 (1989) 50.

- [12] Y.-K. Shin, U. Ewert, D.E. Budil and J.H. Freed, *Biophys. J.* 59 (1991) 950.
- [13] W.A. Edelstein, J.M.S. Hutchinson, G. Johnson and T. Redpath, *Phys. Med. Biol.* 25 (1980) 751.
- [14] J. Gorcester and J.H. Freed, *J. Chem. Phys.* 85 (1986) 5375.
- [15] J. Gorcester and J.H. Freed, *J. Chem. Phys.* 88 (1988) 4678.
- [16] J. Gorcester, G.L. Millhauser and J.H. Freed, in: *Modern pulsed and continuous-wave electron spin resonance*, eds. L. Kevan and M. Bowman (Wiley, New York, 1990) ch. 3.
- [17] B.R. Patyal, R.H. Crepeau, D. Gamliel and J.H. Freed, *Chem. Phys. Letters* 175 (1990) 445.
- [18] B.R. Patyal, R.H. Crepeau, D. Gamliel and J.H. Freed, *Chem. Phys. Letters* 175 (1990) 453.
- [19] A. Angerhofer, R.J. Massoth and M.K. Bowman, *Israel J. Chem.* 28 (1988) 227.
- [20] M. Bowman, in: *Modern pulsed and continuous-wave electron spin resonance*, eds. L. Kevan and M. Bowman (Wiley, New York, 1990) ch. 1.
- [21] M.K. Bowman, *Bull. Am. Phys. Soc.* 31 (1986) 524.
- [22] J. Gorcester, G.L. Millhauser and J.H. Freed, *Magn. Reson. Related Phenom., Proc. Congr. Ampere*, 23rd (1986) 562.
- [23] O. Dobbert, T. Prisner and K.P. Dinse, *J. Magn. Reson.* 70 (1986) 173.
- [24] J. Prisner, O. Dobbert, K.P. Dinse and H. van Willigen, *J. Am. Chem. Soc.* 110 (1988) 1623.
- [25] A. Angerhofer, M. Poporowicz, M.K. Bowman, J.R. Norris and H. Levanon, *J. Phys. Chem.* 92 (1988) 7164.
- [26] U. Ewert, R.H. Crepeau, S. Lee, C.R. Dunnam, D. Xu and J.H. Freed, *Chem. Phys. Letters* 184 (1991) 34.
- [27] G.R. Eaton and S.S. Eaton, in: *EPR imaging and in vivo EPR*, eds. G.R. Eaton and S.S. Eaton (CRC Press, Boca Raton), in press.
- [28] G.G. Maresch, M. Mehring and S. Emid, *Physica B* 138 (1986) 261.
- [29] A.D. Milov, A. Yu. Pusep, S.A. Dzuba and Yu.D. Tsvetkov, *Chem. Phys. Letters* 119 (1985) 421.
- [30] D.J. Sloop, H.-L. Yu and T.-S. Lin, *Chem. Phys. Letters* 124 (1986) 456.
- [31] B.H. Suits and D.E. Wilken, *J. Phys. E* 22 (1989) 565.
- [32] A. Schweiger, in: *Modern pulsed and continuous-wave electron spin resonance*, eds. L. Kevan and M. Bowman (Wiley, New York, 1990) ch. 2.
- [33] J.P. Hornak and J.H. Freed, *Chem. Phys. Letters* 101 (1983) 115.
- [34] S.A. Dzuba, A.G. Maryasov, K.M. Salikhov and Yu.D. Tsvetkov, *J. Magn. Reson.* 58 (1984) 95.
- [35] MacSPICE, Deutch Research Inc., Palo Alto, CA.
- [36] U. Ewert and J.H. Freed, 13th International EPR Symposium, Rocky Mountain Conference, Denver, CO (1990).
- [37] M.J.R. Hoch and U. Ewert, in: *EPR imaging and in vivo EPR*, eds. G.R. Eaton and S.S. Eaton (CRC Press, Boca Raton), in press.